ACS APPLIED MATERIALS & INTERFACES

Research Article

www.acsami.org

Full-Field Synchrotron Tomography of Nongraphitic Foam and Laminate Anodes for Lithium-Ion Batteries

Fikile R. Brushett,*[,†] Lynn Trahey,*[,‡] Xianghui Xiao,[§] and John T. Vaughey[‡]

[†]Department of Chemical Engineering, Massachusetts Institute of Technology, Cambridge, Massachusetts 02139, United States

[‡]Chemical Sciences & Engineering Division, Argonne National Laboratory, Argonne, Illinois 60439, United States

[§]Advanced Photon Source, Argonne National Laboratory, Argonne, Illinois 60439, United States

Supporting Information

ABSTRACT: Nondestructive methods that allow researchers to gather high-resolution quantitative information on a material's physical properties from inside a working device are increasingly in demand from the scientific community. Synchrotron-based microcomputed X-ray tomography, which enables the fast, full-field interrogation of materials in functional, real-world environments, was used to observe the physical changes of next-generation lithium-ion battery anode materials and architectures. High capacity, nongraphitic anodes were chosen for study because they represent the future direction of the field and one of their recognized limitations is their large volume expansion and contraction upon cycling, which is responsible for their generally poor electrochemical performance. In this work, Cu_6Sn_5 coated on a three-dimensional copper foam was used to model a high power electrode while laminated silicon particles were used to model a high energy electrode. The electrodes were illuminated *in situ* and *ex situ*, respectively, at Sector 2-BM of the Advanced Photon Source. The changes in electrode porosity and surface area were measured and show large differences based on the electrode architecture. This work is one of the first reports of full-field synchrotron tomography on high-capacity battery materials under operating conditions.

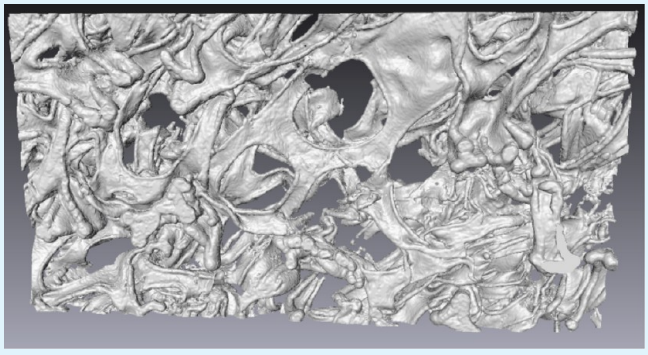

KEYWORDS: *MicroCT, synchrotron tomography, Li-ion anodes, silicon, Cu_6Sn_5*

1. INTRODUCTION

Rechargeable lithium-ion batteries (LIBs) are portable electrical energy storage devices which have dominated the consumer electronics market for the past 20 years.[1] Translating this success to the transportation market requires doubling the battery energy density without increasing cost or sacrificing safety.[2] A key limitation to developing the next-generation of energy storage systems is derived from the inherent shortcomings of graphitic carbon used as a negative electrode (or anode) in today's LIBs, namely, its low gravimetric (372 mAh/g) and volumetric (818 mAh/cm^3) capacity. Over the past decade, various classes of materials have been proposed and studied as alternative anodes, most notably, (i) metals (e.g., Sn), (ii) metalloids (e.g., Si, Ge), (iii) intermetallic compounds (e.g., CoSn, Cu_6Sn_5), and (iv) metal oxides (e.g., CoO, $Li_4Ti_5O_{12}$). Metals, metalloids, and intermetallic compounds are of particular interest because they offer significantly higher theoretical volumetric and gravimetric capacities compared to graphitic carbon while operating at similar potentials. For example, Si can accommodate nearly four lithium atoms per unit, providing a theoretical gravimetric and volumetric capacities of 4009 mAh/g and 9339 mAh/cm^3 ($Li_{4.25}Si$) and operating between ca. 0.01 and 0.5 V vs Li^0/Li^+.[3]

Despite their advantages, high capacity materials have not supplanted graphitic carbon as the dominant commercial materials due to mechanical problems associated with the significant volume changes (often >300%) which accompany lithium insertion and removal. These volume shifts cause particle pulverization (until some critical particle size is reached based on stress/strain relations) which results in continuous exposure of fresh surfaces to electrolyte, leading to increased solid-electrolyte interphase (SEI) passivating layer formation and the eventual electronic isolation of active materials within the electrode structure.[4] This anode volume shift can lead to electrode level failure due to polymeric binder breakdown and electrode delamination from the current collector. While significant research efforts have focused on designing electrodes that can accommodate these volume shifts without sacrificing capacity, success has been limited. To date, several approaches, including new polymer binders,[5−7] nanostructured materials and composites,[8−11] and microstructured electrode architectures[12−14] have been reported. In addition, new operating

Received: January 15, 2014
Accepted: March 3, 2014
Published: March 3, 2014

   dx.doi.org/10.1021/am5003124 | ACS Appl. Mater. Interfaces 2014, 6, 4524−4534

protocols have been proposed such as capacity-limited cycling to extend the electrode lifetime by minimizing the lithium inserted per silicon and thus the volume shifts.[15,16] While all of these approaches have yielded promising results, cell-level performance with realistic active-materials loadings still falls short of established capacity and lifetime targets.

Gaining a better understanding of electrode microstructure and, more specifically, the electrically- and chemically driven changes to that structure over electrode lifetime is key to designing next-generation energy storage systems. To this end, a number of microscopies and spectroscopies have been employed to probe physical and chemical changes in battery materials. Microcomputed X-ray tomography (MicroCT) is an emerging analytical technique that measures variation in X-ray attenuation upon rotating samples, to generate three-dimensional maps of samples with high spatial resolution (1−10 μm) in a nondestructive fashion over large geometric volumes (on the order of 1 mm^3). Variations in X-ray absorption enable identification of different phases/elements and their distribution, throughout the sample. Three-dimensional imaging of complex electrode architectures provides detailed information about structural organization, species location, and local physical properties (e.g., porosity, tortuosity). A better understanding of the changes in these physical properties can play a large role in improving modeling and simulation efforts that draw out relationships between microstructure and performance.[17]

The nondestructive nature of MicroCT enables *operando* imaging of electrochemically driven morphological changes in three dimensions provided these temporal processes are slower than the image collection rate. While laboratory-scale MicroCT systems have limited collection rates, on the order of 1−2 h, high speed synchrotron-based MicroCT enables image collections in as little as 15 s without sacrificing resolution. Although MicroCT enables visualization of electrode microstructure (down to a volumetric pixel, or voxel, size of 1 μm^3), analysis of the nanoscale materials (e.g., primary particles) requires the use of complementary techniques with higher spatial resolution such as focused-ion beam scanning electron microscopy (FIB-SEM),[18−20] transmission electron microscopy (TEM),[21−23] or nanocomputed X-ray tomography (NanoCT).[24−26] However, in most cases, these techniques generally require destructive sample preparation (e.g., ion-milling sections of a larger electrode) or the use of nanostructured materials, such as single nanowires.[27] In addition, deviations from typical benchtop behavior of electrochemical cells from X-ray and electron beam interactions are an emerging concern which have been highlighted in the fuel cell community.[28,29] A deeper reflection of this issue as it pertains to our experiments will follow.

While significant efforts have focused on using MicroCT to characterize porous materials for energy conversion applications (i.e., fuel cells),[30−40] fewer efforts have focused on porous electrochemical energy storage applications. Fukunaga et al. used MicroCT to characterize electrode swelling and distortion within sealed cylindrical nickel−metal hydride cells after cycling.[41] Manke et al. employed synchrotron tomography, in combination with neutron tomography, to probe changes in the three-dimensional spatial distribution of different chemical components inside primary alkaline Zn-MnO_2 batteries during discharge.[42] Haibel et al. expanded on this earlier work by using *in situ* microtomographic imaging to study the physical changes which occur during discharge of a commercial AAAA Zn-MnO_2 battery.[43] More recently, Brandon and co-workers have begun to utilize multiscale tomography analysis for characterizing various aspects of rechargeable LIBs including an excellent perspective article.[44−47] However, to date, research efforts have focused on characterizing present day LIB materials (i.e., graphite anodes and metal oxide cathodes); MicroCT is perhaps even better suited for investigating the high capacity metal and metalloid active materials for the next-generation LIBs because, as compared to graphite, these materials have a high X-ray absorption and large volume changes during charge and discharge.

Here, we employ synchrotron-based, full-field MicroCT to characterize two different nongraphitic anode materials: an engineered microporous copper−tin composite and a more traditional silicon-based laminate. We perform *ex situ* studies on both materials before and after cycling to visualize three-dimensional structural changes and determine key physical properties. In addition, we have developed a proof-of-concept electrochemical cell for simultaneous microtomographic and electrochemical measurements to directly correlate changes in physical structure to shifts in electrochemical performance. We perform *operando* studies on the microporous Cu−Sn composites to better understand lithiation processes and subsequent structural evolutions throughout the three-dimensional architecture. These *ex situ* and *in situ* studies of high-capacity materials highlight a number of failure mechanisms which would have been difficult to determine via complementary methods. Furthermore, we hope these initial studies will highlight the utility of MicroCT as a tool for electrode characterization and spur greater use of the technique throughout the energy storage community.

2. EXPERIMENTAL SECTION

2.1. Electrode Preparation. In this study, two fundamentally different electrodes were characterized: copper−tin on copper (Cu_6Sn_5 on Cu) foam (high power) electrodes and traditional laminated (high energy) silicon (Si laminate) electrodes. Cu_6Sn_5 on Cu foam electrodes were made by the electroless plating of tin, using a Caswell plating solution, onto copper foam sheets (90 ppi, 380 g/m^2 areal weight, 1.5 mm thickness, Circuit Foil). Prior to tin plating, the foams were calendared to 100 μm thickness and washed with dilute hydrochloric acid and acetone. Copper foam porosity was measured before and after calendering. Electroless tin plating was performed for roughly 1 min in two 30 s intervals at 50 °C with no agitation. Submersion of the foam in the bath immediately coats the copper with tin, as evidenced by the color change from orange to gray. The electrodes, both carbon- and binder-free, were rinsed with deionized water and dried with a heat gun (estimated T < 100 °C) at a considerable distance. Si laminate electrodes were prepared using 70 wt % Si particles (325 mesh, Aldrich), 20 wt % polyvinylidene difluoride (PVDF, Aldrich), and 10 wt % Super P Li carbon (Timcal). *N*-Methyl-2-pyrrolidone (NMP, Aldrich) was added to control the slurry viscosity. The slurry was cast with 200 μm thickness onto copper foil via a doctor blade. To remove the NMP, the resulting laminate was first dried in an oven at 75 °C and then dried overnight in a vacuum oven at 65 °C.

2.2. Electrochemical Testing. Electrochemical performance of the two electrodes was first evaluated in stainless steel coin cells (Hohsen 2032). Unless specified otherwise, the Cu_6Sn_5 on Cu foam and Si laminate electrodes were punched into 1/2 in. (12.7 mm) discs and cycled vs 1/2 in. Li metal (FMC Lithium) separated by a single 5/8 in. (~15.9 mm) Celgard (2325) separator. In all studies, the electrolyte used was 1.2 M $LiPF_6$ in 3:7 wt % ratio ethylene carbonate/ethyl methyl carbonate (Tomiyama High Purity Chemical Industries Ltd.). All coin cells were tested on a MACCOR cycler (Series 4000).

2.3. Scanning Electron Microscopy and X-ray Diffraction. Cu_6Sn_5 on Cu foam electrodes were analyzed via scanning electron microscopy (SEM, JEOL 6400), energy-dispersive X-ray spectroscopy (EDS, Oxford INCA), and X-ray diffraction (XRD, Siemens D5000, Cu Kα radiation).

2.4. Beamline Cell Assemblies and Testing. An electrochemical cell was constructed to enable simultaneous electrochemical analysis and microtomographic imaging. The cell housing consisted of X-ray transparent, electrically insulating polyamide-imide (Torlon, McMaster-Carr) which was precision-machined into a 5 mm outer diameter tube with an inner diameter threaded throughout to enable stainless steel screws (4−40, McMaster-Carr) to secure, seal, and apply pressure to the cell stack. The cell stack consists of a 5/64 in. (~1.98 mm) diameter Cu_6Sn_5 on Cu foam electrode and a 5/64 in. (~1.98 mm) diameter Li metal electrode separated by a 3/32 in. (~2.38 mm) diameter Celgard 2325 separator or glass fiber separator (Whatman GF/F). All cell components were stored and punched in an argon-filled glovebox and presoaked in the electrolyte. However, due to the small size and delicate nature of the electrolyte-soaked components, the cell was rapidly assembled and sealed outside of the glovebox on the laboratory benchtop. In addition to the screws, the tube ends were sealed with Parafilm. Figure 1a shows a schematic and photograph of the assembled beamline cell. Prior to transportation to the synchrotron, electrochemical analyses were performed on the cells using a portable potentiostat (Gamry Reference 600). For all cells, open circuit potential was monitored for one hour to ensure no short circuiting had occurred during assembly. For some of the cells, cyclic voltammetry was also performed to verify reduction and oxidation characteristics.

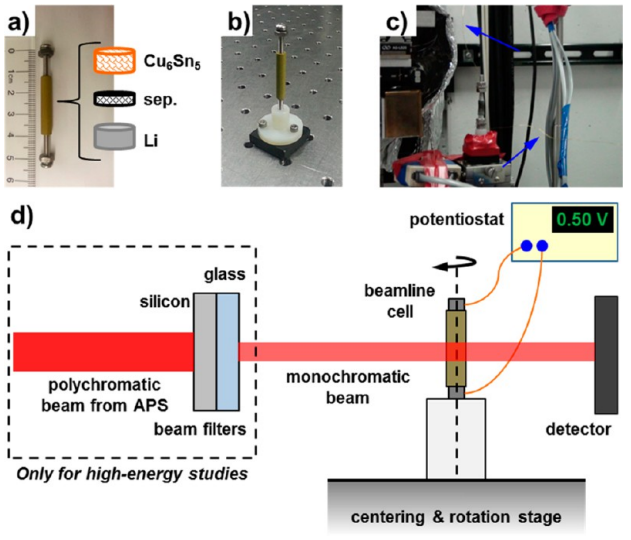

Figure 1. (a) Beamline stack schematic consisting of a lithium metal electrode (gray), a porous separator (crosshatched black and white), and the electrode of interest, represented as Cu_6Sn_5 on Cu foam here (crosshatched orange and white). (b) The cell is mounted onto a Teflon-based stand which is then magnetically attached to a rotating stage in the beam path. (c) Copper leads are attached to the cell to make an electrical connection to the potentiostat without impacting the cell's ability to rotating freely. (d) Schematic of synchrotron microtomography at the 2-BM beamline of Advanced Photon Source (APS) at Argonne National Laboratory (ANL). For *ex situ* measurements, the electrode of interest was housed in the unconnected cell stack to minimize sample movement during rotation.

At the beamline, the cell is mounted on a threaded Teflon-stand to secure the entire cell assembly via the screws (Figure 1b). The stand is then magnetically attached to the rotation stage in the beamline. Thin unclad copper or brass wires were wrapped around the screws connecting each electrode and were secured between two hex nuts. The wires were then connected to the same Gamry potentiostat (Figure 1c). The wire lengths were long enough to enable the cell to rotate in the beamline without obstruction. During X-ray illumination, electrochemical testing was performed via remotely controlling the potentiostat within the beamline hutch. Figure 1d shows a general schematic of the cell in the 2-BM beamline which is described in detail below.

2.5. Synchrotron-Based Microtomography. The experiments were conducted at the 2-BM beamline of Advanced Photon Source (APS) at Argonne National Laboratory. 2-BM is a dedicated tomography beamline, which utilizes the standard APS bending magnet (BM) source and delivers a usable X-ray spectrum that exceeds 100 keV. The beamline is equipped with double-multilayer mirrors as monochromator (DMM) that can be used when the desired X-ray energy is less than 50 keV. When higher energies are needed, the monochromator is removed. For these higher X-ray energies (>50 keV), the beaming hardening effect, which exists for most commercial CT systems, can be largely reduced with appropriate filtration. In all experiments, we employed an X-ray microscope equipped with a pco.dimax CMOS camera that has 2016 × 2016 pixels of 11 × 11 μm^2 pixel size, a Mitutoyo 10× long-working-distance lens, and a 100 μm thick LAG:Ce scintillator. Therefore, the equivalent pixel size in the projection images is 1.1 × 1.1 μm^2; the equivalent voxel (volumetric pixel) size in the three-dimensional renderings is 1.1 × 1.1 × 1.1 μm^3, and the field of view (FOV) is ca. 2.2 × 2.2 mm^2. However, the actual spatial resolution in the tomographic reconstructions depends not only on the image pixel size but also on the imaging system point spread function and image contrast. The tomographic reconstruction spatial resolution can be estimated on the basis of the edge response function across a sharp feature boundary.[48] According to 10−90% distance,[49,50] the spatial resolution can be estimated as ca. 4.4 μm for both electrodes. This value represents the upper bound of the actual spatial resolution since the feature boundary used in the estimation might not be a perfectly sharp edge.

2.6. Acquisition, Reconstruction, and Segmentation of MicroCT Data. In all studies, the electrodes were secured on the stand and rotated stepwise over 180° within the X-ray beam to generate a series of projection images. For *ex situ* studies, electrodes either were adhered onto a stainless steel screw using carbon tape or were secured in tube cell housing to prevent sample movement during image collection. For *in situ* studies, the electrodes were secured in the operational tube cell. The projection images were then processed to reconstruct a series of 2D tomographic slices. The volumetric analysis based on the slice stack for each electrode was done with the Amira software package (Version 5.3, Visage Imaging).

For the Cu_6Sn_5 on Cu foam electrode experiments, we used the broad X-ray spectrum from 2-BM source with 15 mm Si and 10 mm glass as filters (Figure 1d, including beam filter box). The cutoff energy is ca. 50 keV which is enough to penetrate 2 mm foam. The detector-to-sample distance was 20 mm, so absorption contrast dominates in the projection images. A total of 1500 projection images were captured at a rate of 50 images per second (2 ms exposure time, 6°/s rotational speed). The 3D structure of the foam is reconstructed from the projection images using the gridrec algorithm, a modified filtered-back-projection algorithm.[51,52] The result was output into Amira for volume segmentation from which quantitative analyses of the electrode microstructure, as well as the structural changes during charge/discharge cycling, were extracted. To reduce noise, a two-dimension median filter of size 3 × 3 was applied to the reconstructed slice images. For accurate analysis, a representative analytical volume (1703 pixels × 892 pixels × 100 pixels) is selected on the basis of two criteria: (i) the analytical volume is the majority of the total electrode volume (2016 pixels × 2016 pixels × 100 pixels), and (ii) the analytical volume does not include or is not distorted by either the screw−electrode interface or the electrode−separator interface. The same global threshold was then used to segment the electrode from the surrounding electrolyte in all scans, to maintain segmentation consistency in all scans. For volume specific surface area or surface area to volume ratio (SA/V), the surface area and volume were obtained from Amira directly as two properties of the segmented

electrode. In SA/V, the contribution to the area from the bounding surface of the volume is subtracted so it is only the natural electrode surface included in the calculation. In order to probe whether lithiation/delithiation extent during cycling has variations along the electrode depth direction, we also calculated the SA/V values for the upper half and lower half volumes of the same electrode by repeating the above analysis to these two subvolumes.

For Si laminate electrode experiments, 50 keV monochromatic X-ray with 1.5% bandwidth from the DMM was used (Figure 1d, excluding beam filter box). A total of 1800 projection images were captured at a rate of 3 images per second (100 ms exposure time, 0.3°/s rotational speed). To help differentiate between the Si particles and carbonaceous species, the detector-to-sample distance is set at 100 mm to take advantage of the partial coherence of the X-ray beam and enable propagation phase-contrast imaging. Prior to image reconstruction, a Paganin phase retrieval algorithm is applied to the projection data to enhance the contrast among all material phases and facilitate the use of a single global threshold for segmentation of each material phase.[53] Due to their delicate nature, the Si laminates were easily deformed during beamline sample preparation which challenged uniform analytical volume selection as we did not want to capture exterior empty space above the electrode or copper foil current collector below the electrode. Consequently, slightly different representative analytical volumes were selected for each electrode.

For image analyses for both electrode types, uncertainty may arise from multiple sources including minor heterogeneities between different samples of the same material, changes in the selected analytical volume which may lead to the inclusion of different amounts of void space, and noise inherent to the image collection which can induce some uncertainty in segmentation. Depending on the property of interest, each of these sources of error may play a different role. For example, in the case of bulk porosity estimation, variations in selected analytical volume are the most likely source of error. We account for and attempt to minimize these errors by maintaining consistency in sample preparation, data collection, and image processing parameters. Moreover, whenever possible, computed values are compared to experimentally obtained values.

3. RESULTS AND DISCUSSION

3.1. Cu_6Sn_5 on Cu Foam Electrodes. *3.1.1. Structural Investigations.* Microporous metal foams hold several key advantages as substrates for rechargeable battery electrodes. First, the foam can act as a porous current collector which traverses the electrode thickness and enhances through-plane electronic conductivity while enabling the electrode to function in a dual-sided manner (if desired). Second, the foam can act as a conductive substrate for the direct deposition (e.g., electrodeposition, electroless deposition) of high capacity intermetallic, metallic, or metalloid active materials which eliminates the need for conductive additives and binders. This may offer opportunities for simplified high throughput electrode syntheses at the large scale. Third, the porous nature of the foam provides sufficient void volume not only to accommodate the volumetric expansion of these high capacity materials but also to provide adequate space for the SEI to remain intact at the bottom of the charge. Fourth, the porous nature of the foam also facilitates electrolyte percolation and ionic conductivity throughout the entire electrode structure which may enhance rate capabilities (power) and enable thicker more energy dense electrodes. The key is to optimize the balance of active materials, void volume, and thickness to maximize performance and durability for a particular application.

In general, while the Cu foam used here has a lower surface area and higher weight per unit area than desirable for high performance batteries, the porous electrodes created have value for scientific investigations of electroless deposition uniformity and active layer formation, stability, and electrochemical activity (Figure 2a). The as-received foam was calendered from a 1.5 mm thickness to a 100 μm thickness to densify the structure (Figure 2b,c). The compression decreased the foam porosity from ca. 97% to ca. 60% and flattened the diamond-shaped wiring into sheets with slightly increased thickness on the edges. The Sn was then plated onto the Cu foam via an electroless deposition bath to form a somewhat conformal layer a few micrometers thick (Figure 2d). The process immediately turned the foam from orange to gray. XRD spectra of electrodes were strongly dominated by Cu signal with a small peak ca. 30°. 2θ indicates the hexagonal bronze, electrochemically active Cu_6Sn_5, and no Sn peaks. The Sn peaks were detected with longer electroless deposition times; however, these samples were not used in this particular study. EDS analysis of the electrodes detected Cu and Sn along with small carbon and oxygen impurities.

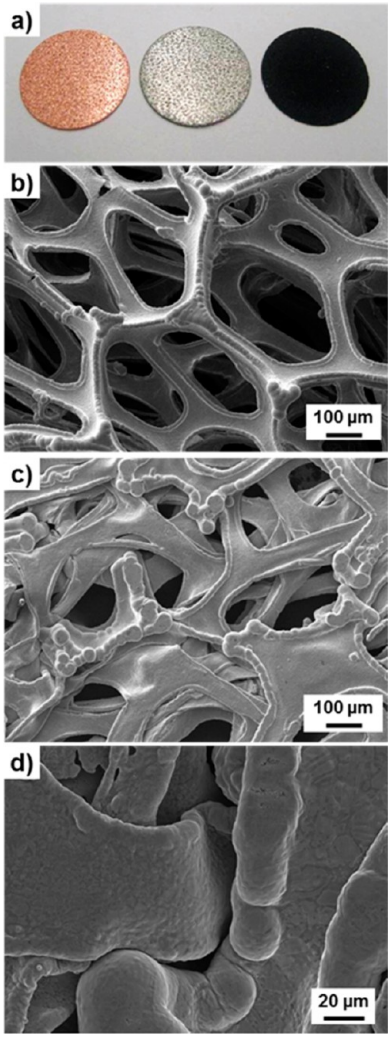

Figure 2. (a) Digital photographs, from left to right, of the Cu foam, the foam after Sn electroless deposition, and the foam after extended electrochemical cycling in a Li half-cell. The SEM images show (b) the as-received Cu foam, (c) the calendered Cu foam, and (d) the Cu foam after conformal Sn deposition. The electrode area averaged 13 at % Sn with the balance being Cu (as measured by EDS).

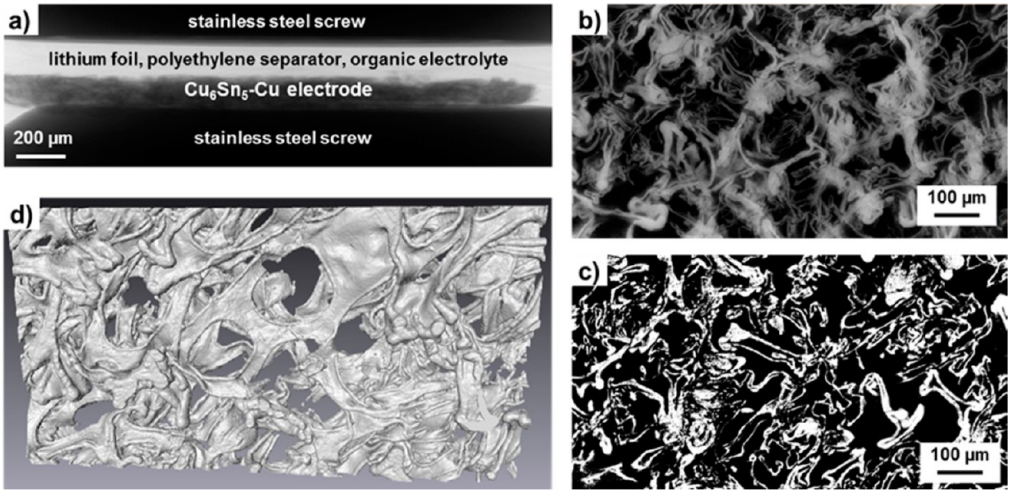

Figure 3. (a) An X-ray projection image of the electrode|separator|electrode assembly within the beamline cell. (b) An example of a grayscale 2D unsegmented radiographic cross-section of the Cu_6Sn_5 on Cu foam electrode. (c) An example of a 2D binary segmented (white, material; black, void) radiographic cross-section of the same Cu_6Sn_5 on Cu foam electrode obtained via thresholding analysis. (d) After segmentation, filament tracing is used to connect materials throughout the radiograph stack and generated a 3D model of Cu_6Sn_5 on Cu foam. The pixel size in the radiographic images is 1.1 × 1.1 μm^2, and the voxel size in the 3D renderings is 1.1 × 1.1 × 1.1 μm^3.

Microtomographic imaging enables nondestructive three-dimensional characterization of the electrode providing information about internal structure, species distribution, and physical properties (e.g., porosity). Figure 3 shows a flowchart of image acquisition and processing. Figure 3a shows a projection image of electrode|separator|electrode assembly within the beamline cell stack in the APS. While the Cu_6Sn_5 on Cu foam electrode is clearly visible, at the experimental X-ray energy (ca. 50 keV), the porous plastic separator and Li-electrode have very low absorption due to their low atomic number and thus appear nearly invisible. As the cell stack rotates in the beamline, a series of projection images are captured and reconstructed into 2D radiographic images. Figure 3b shows a grayscale 2D radiographic cross-section of the Cu_6Sn_5 on Cu foam electrode which reveals an intricate internal structure with fine features. As the radiograph represents a 1.1 μm thick slice of the electrode layer, these features can be attributed to morphological variations on the surface of the larger compressed Cu branches (widths $\geq$50 μm). All of these pore structures may not be equally accessible as compression of the Cu nodes may trap some pockets. To generate a quantitative 3D rendering, the grayscale radiographs must be segmented into 2D binary images (Figure 3c) which identify and separate voxels predominantly filled with materials (white) from those that are predominantly void (black). Direct differentiation of the active Cu_6Sn_5 layer from the Cu foam substrate is not possible because of the weak contrast between the Cu and Sn at the experimental X-ray energy and because the Sn film thickness is on the same order of the imaging resolution. Segmentation is performed via a combined approach of thresholding and filament tracing methods.[36] After segmentation, in the third and final step, a 3D reconstructed volume of these binary images is used for subsequent quantitative analysis (Figure 3d). For example, the porosity ε is defined as: $\varepsilon = 1 - (\text{material}_{vox})/(\text{material}_{vox} + \text{void}_{vox})$, where material_{vox} is the number of material voxels filled with Cu_6Sn_5, and Cu (both are assumed to be impermeable) and void_{vox} is the number of void voxels. Analysis of microtomographic images reveals a foam porosity of 57 ± 4% (N = 18) which is near-identical to that measured on the benchtop. This indicates that the 3D segmentation accurately captures bulk material properties and the selected analytical volume is sufficiently large to represent these properties. Moreover, the pore structure is interconnected with no isolated/broken pieces which suggests good ionic and electronic conductivity throughout.

3.1.2. Electrochemical Investigation. To confirm the electrochemical activity, the Cu_6Sn_5 on Cu foam electrodes was cycled in coin cells vs Li metal. Figure 4 shows representative cycling voltage profiles of the first few cycles of a 2 mm diameter Cu_6Sn_5 on Cu foam, the size of the electrodes to be used in the beamline cell, vs 9 mm diameter Li counter electrode, separated by a single 2325 Celgard. Lithiation (discharge) and delithiation (charge) were galvanostatically controlled at 20 μA between 1.5 and 0.01 V. The lithiation plateau at 400 mV (vs Li^0/Li^+) is indicative of the Cu_6Sn_5 phase.[54,55] Significant hysteresis in the lithiation and delithiation processes is evident, as is typical. In these coin cell configurations, the foam electrodes displayed stable cycle behavior for 20–30 cycles before decay. Figure 2a (see above) shows a digital image of a post-mortem black Cu_6Sn_5 on Cu

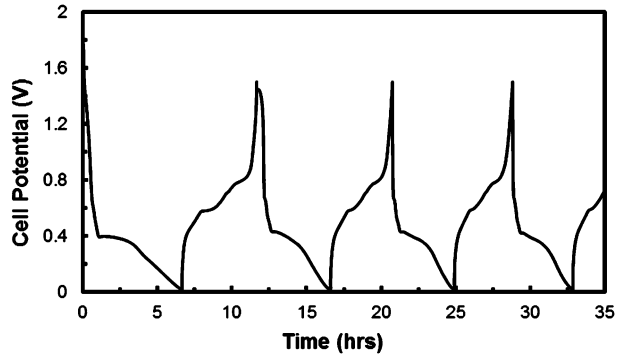

Figure 4. Representative charge–discharge cycle profiles at 20 μA between 0.01 and 1.5 V of a coin cell containing a 2 mm Cu_6Sn_5 on Cu foam electrode and a 9 mm Li metal electrode separated by a single 2325 Celgard.

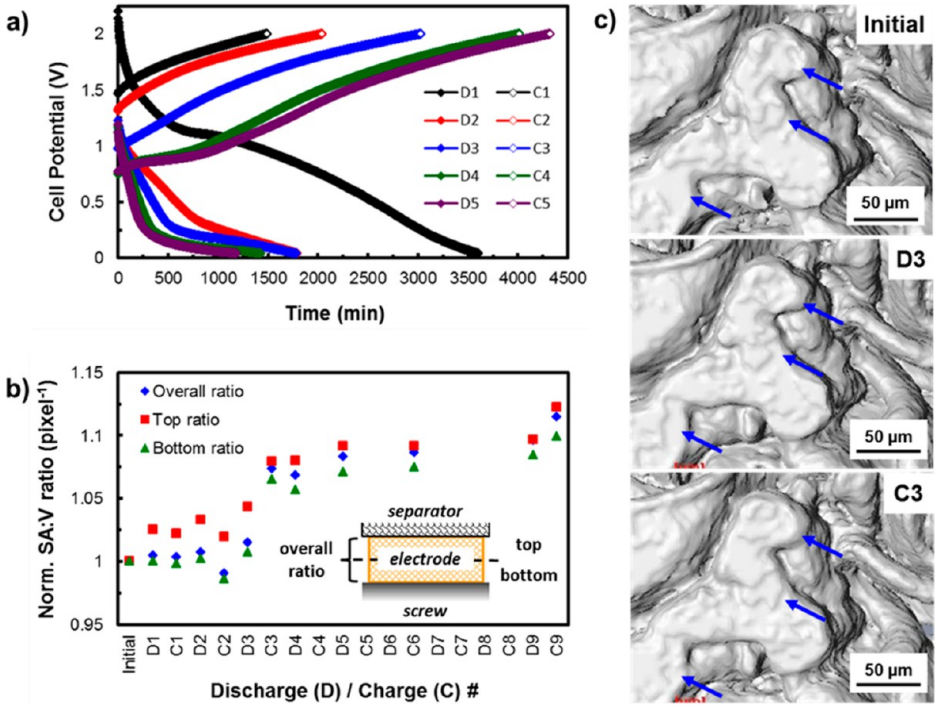

Figure 5. (a) First 5 discharge (lithiation)/charge (delithiation) cycles for the beamline cell A with electrode|separator|electrode stack consisting of a Cu_6Sn_5 on Cu foam electrode, a single 2325 Celgard separator, and a Li-metal electrode. Cell was cycled between 0.01 and 2 V, and the discharge and charge currents were 10 and 1 μA, respectively. (b) Changes of surface area-to-volume (SA/V) ratio of the total electrode, the upper half (from the mid-electrode to the electrolyte interface) and the lower half (from mid-electrode to the current collector interface) as a function of cycle number and discharge/charge state. Each volume specific surface area is normalized to its initial value. (c) Qualitative representative MicroCT renderings of a distinctive electrode feature initially, after the third discharge, and after the third charge. The blue arrows are intended to draw the eye to areas of marked topological change.

foam (on the right). Additional SEM images of the post-mortem foam can be found in the Supporting Information (Figure S1).

The nondestructive nature of MicroCT imaging enables *operando* electrode analysis provided that the morphological changes occur on a time scale slower than the image collection rate. While this is a challenge for laboratory-scale MicroCT systems, which have collection rates on the order of 1−2 h, high speed synchrotron-based MicroCT systems can collect full-field images in as little as 15 s without sacrificing resolution. As mentioned before, while direct differentiation of the active Cu_6Sn_5 layer is not possible, during lithiation and delithiation, subtle shifts in the Cu_6Sn_5 layer morphology can still be observed and quantified via appreciable changes in surface area-to-volume (SA/V) ratio. To this end, two beamline cells, Cells A and B, were cycled at the APS and changes to their SA/V ratio characterized. Prior to transportation to the beamline, cyclic voltammetry and charge/discharge studies were performed to determine cell characteristics (Supporting Information Figure S2). In general, the behavior of the beamline cells demonstrated higher resistivities and lower reproducibility than the standard coin cells which is currently attributed to variable stack pressure. Figure 5a illustrates the electrochemical response to galvanostatic cycling of Cell A. To witness (draw out) a reaction plateau on charging (delithiation) cycles, the discharge current density was lowered by roughly an order of magnitude (i.e., 10−20 μA discharge, 1−5 μA charge) for the *in situ* cell. Overall, the cell discharge plateaus grew progressively shorter over the first 5 cycles whereas the cell charge plateaus grew progressively longer. Substantial SEI formation in the first lithiation leads to poor first cycle Coulombic efficiency. Interestingly, the onset potential charge curves also lower from ca. 1.5 to 0.75 V over the first five cycles. This unusual cycle behavior is likely due to a significant SEI formation in combination with limited electrolyte volume. In addition, CT radiation-induced electrolyte reduction may play a role in increasing SEI formation. Indeed, Shkrob et al. have recently shown that radiolysis of electrolytes can cause SEI formation in the absence of electrochemical cycling.[56] Although a functional electrical connection is maintained throughout the *operando* tomography, significant resistance exists between the positive and negative electrode terminals of the beamline cell which is attributed to electrolyte leakage, to radiation-induced changes in the electrolyte, and to unregulated cell pressure. For comparison, similar charge−discharge experiments were run on a second beamline cell, Cell B, which replaced the Celgard polypropylene-based film with a quartz microfiber (Whatman) separator (Supporting Information Figure S3). The fiber was found to hold more electrolyte solution and to contour to the electrodes, giving a better electrochemical response than the Celgard separators (more similar to coin cell responses). Despite this unusual behavior of this proof-of-concept cell, lithiation events still occur in the expected voltage regime indicating that the Cu_6Sn_5 in Cu foam electrode is functional and thus *operando* morphological analyses are of value.

Figure 5b shows the changes in normalized SA/V ratio as a function of cycle number for Cu_6Sn_5 on Cu foam electrode within the beamline cell. As mentioned above, to minimize the impact of beam-induced electrolyte reduction, the cell was only illuminated when CT scans were performed (~30 s each). The extended delithiation (charge) plateaus observed in the fourth and fifth cycle (see Figure 5a) correspond to cycles where the

dx.doi.org/10.1021/am5003124 | ACS Appl. Mater. Interfaces 2014, 6, 4524−4534

MicroCT scans were omitted suggesting that X-ray illumination plays some role in cell behavior. Although not as extensively characterized, similar trends were observed for Cell B. This relationship merits extra consideration for practitioners of high energy electron and X-ray studies and will be explored in greater detail in a future publication. SA/V ratios were characterized for the total electrode, the upper-half of the electrode (from mid-electrode to the electrolyte interface), and the lower-half of the electrode (from mid-electrode to the current collector interface) to determine if the impact of cycling varied as a function of depth into the electrode. Earlier studies by Trahey et al. on porous Cu_2Sb electrodes had shown a variation in SEI formation and electrode resistivity as a function of electrode depth.[4] More specifically, higher resistance was observed at higher altitude electrode surfaces (areas closer to the counter electrode) suggesting increased SEI formation and overall poorer performance. If such an effect is presented in the porous Cu_6Sn_5 on Cu electrodes, this would be reflected in differences in the SA/V ratio on the lower-half of the electrode compared to the top half due to the combination of Sn pulverization and SEI growth. Trahey et al. also showed evidence of morphological changes based on altitude, with caking of the surface (lowering of surface area) evident in highly resistive areas.[4] However, surface areas are expected to increase when the starting electrode surfaces, such as the ones used herein, are smooth. The SA/V ratios were each normalized to their initial values to determine changes from the start of cycling. Over the first couple of charge and discharge cycles, only a slight increase in the SA/V formation on the upper half of the electrode was observed. This increase occurred on the first cycle suggesting initial SEI formation. As noted by Shearing et al., as CT scans are limited to micrometer resolution (ca. 4.4 μm), nanoscale evolutions in the SA/V ratio may be occurring over the first few cycles which are not captured in these measurements.[46] Upon the third cycle, marked increases in all the SA/V ratios were observed due to continued expansion and contraction of the active material. While the upper half the electrode appears to have a slightly higher SA/V ratio than the lower half, a sharp increase in volumetric specific surface area on the third cycle is observed throughout the entire electrode suggesting that electrolyte, and more specifically Li ions, can percolate through the entire electrode structure. This may enable the use of thicker electrodes based on foam current collectors as thicker traditional laminates lack the porosity, and thus electrolyte, in the bulk to support high currents. Note that, though the SA/V ratio did change by 10−15% over the course of electrochemical cycling, because the active layer is significantly thinner than the electrode pore diameters, negligible changes were observed in total electrode porosity and tortuosity. Figure 5c qualitatively demonstrates the topological changes over electrochemical cycling on a representative feature within the Cu_6Sn_5 on Cu foam electrode. Additional qualitative MicroCT images can be found in the Supporting Information (Figure S4). Over the course of several discharge/charge cycles, clear morphological evolutions are observed which, coupled with the electrochemical data, indicate lithiation/delithiation events, which are being observed in this new way for the first time.

3.2. Silicon Laminate Electrodes. The current trends in Si anode research point toward nanophase active materials due to the favorable ionic conduction and high strain tolerance. However, owing to the limiting instrument resolution and a desire to detect electrode destruction, a Si laminate was made from 325 mesh Si (particle size <44 μm) which, being in the micrometer size range, is known to cycle poorly.[57] We chose the laminate percentages of 70 wt % Si, 20 wt % binder, and 10 wt % carbon to mimic reasonable research laminate distributions. Figure 6a,b shows top-down and cross-section

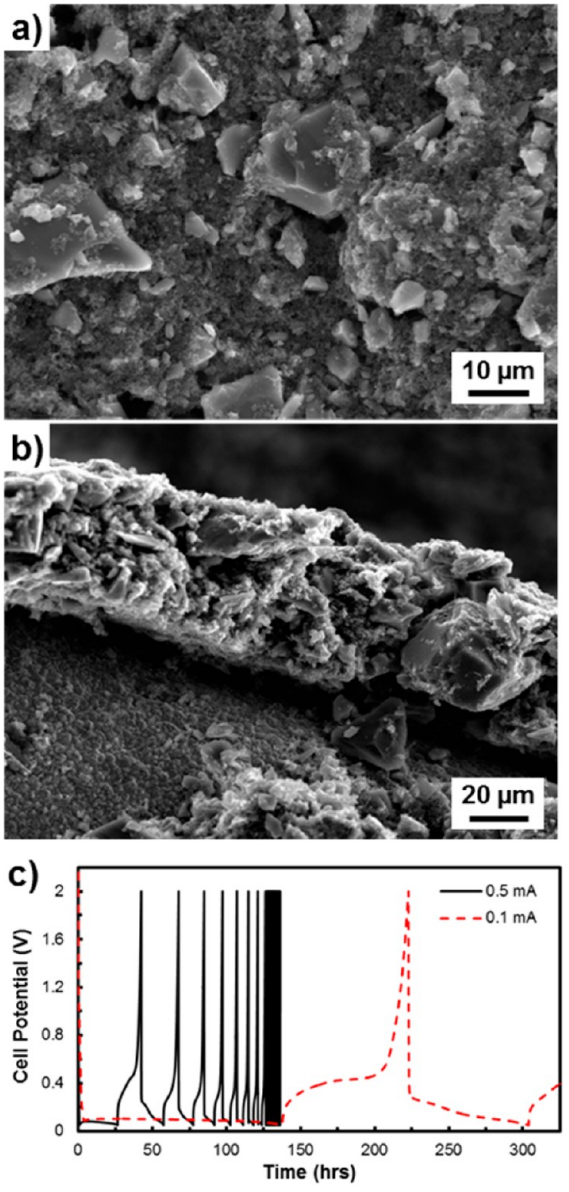

Figure 6. (a) Top-down and (b) cross-sectional SEMs of Si laminate electrode which consist of Si particles, carbon, and PVDF binder. (c) Representative charge−discharge cycle profiles at 0.5 and 0.1 mA between 0.01 and 2 V of a coin cell containing a 12.7 mm Si laminate electrode and a 12.7 mm Li metal electrode separated by a single 2325 Celgard.

SEM micrographs of the pristine laminates with the large Si particles clearly evident. SEM and caliper measurements gave an initial electrode thickness of ca. 80 μm. Figure 6c shows typical coin cell cycling voltage profiles for the composite laminate electrodes at two different current densities (80 and 390 $\mu A/cm^2$). The electrodes demonstrated characteristically high lithiation capacities for the first cycle, poor first cycle Coulombic efficiency, and very short lifetimes when cycled at higher currents. The cells cycled in this current/area range all

dx.doi.org/10.1021/am5003124 | ACS Appl. Mater. Interfaces 2014, 6, 4524−4534

exhibited high initial gravimetric capacity and rapidly diminishing capacity. Additional SEM images of the Si laminates, before and after cycling, can be found in the Supporting Information (Figure S5).

Tomographic scans were performed on the pristine and *ex situ* cycled Si laminates. The harvested laminates were washed with dimethyl carbonate and air-dried before adding to the tomography cell fixture. In some instances, the tomography sample needed to be punched from the harvested laminate. In these cases, the laminate was observed to hold very weakly onto the Cu substrate throughout the process. Consequently, the laminates were handled with great care and no attempts were made to flatten the structures as not to artificially alter the results. When calculating these material properties, a representative analytical volume is selected for each sample based on two criteria: (i) the analytical volume is the majority of the total electrode volume and (ii) the analytical volume does not include or is not distorted by either the Cu foil−laminate interface or the electrode−air (or separator) interface. For the pristine sample, the analytical volume is 340 pixels × 178 pixels × 24 pixels of the total volume of about 1000 pixels × 1000 pixels × 24 pixels, and for the *ex situ* cycled Si laminate sample, the analytical volume is 346 pixels × 318 pixels × 65 pixels of the total volume of about 1000 pixels × 2000 pixels × 110 pixels.

Illustrated in Figure 7a, unlike the Cu_6Sn_5 on Cu foam, the various components of the Si laminate electrode can be qualitatively differentiated at the experimental X-ray energy (50 keV). To better differentiate the Si particles, the carbonaceous materials, and the void spaces within the laminate, the sample-to-detector distance was set at 100 mm to leverage the partial coherence of the X-ray beam and enable propagation phase-contrast imaging. As shown in Figure 7b, phase-contrast imaging enabled the subtle difference in X-ray absorption of each component to be quantitatively differentiated. After phase retrieval, a clear delineation of the particle edge can be made enabling accurate particle quantification and thus segmentations (Figure 7c). Similar phase-contrast processes can be used to differentiate carbonaceous materials from void space. Note that, as before, these analyses are limited by resolution (4.4 μm); thus, features and structural changes occurring below this limit cannot be captured.

Figure 8 shows the segmented microtomographs of the pristine and cycled Si laminate electrodes in the left and right column, respectively, with the distribution of Si particles (purple), carbonaceous materials (green), and voids (red) mapping throughout the 3D composite. From the same laminate, the microtomographs represent two different punches, one pristine and the other cycled in a coin cell until failure and then harvested (see Figure 6c). Post-mortem analyses shows that electrochemical cycling causes the pulverization of the large Si particles (Figure 8a) to smaller distributed particles (Figure 8e), the increase of carbonaceous materials, most likely SEI growth after the pulverized particles and possibly electronically isolated lithiated silicon (Figure 8b−f), and the growth of void space within the electrode (Figure 8c−g). It is important to note that the cycled electrode is significantly thicker than the pristine electrode. This can be attributed to the low packing density of pulverized, SEI-coated Si particles which leads to a thicker, SEI-rich electrode.

Figure 9 shows the cross-sectional orthoslice of the pristine and cycled electrodes. Not only do these qualitative images clearly show the expected changes in the Si particles size, but

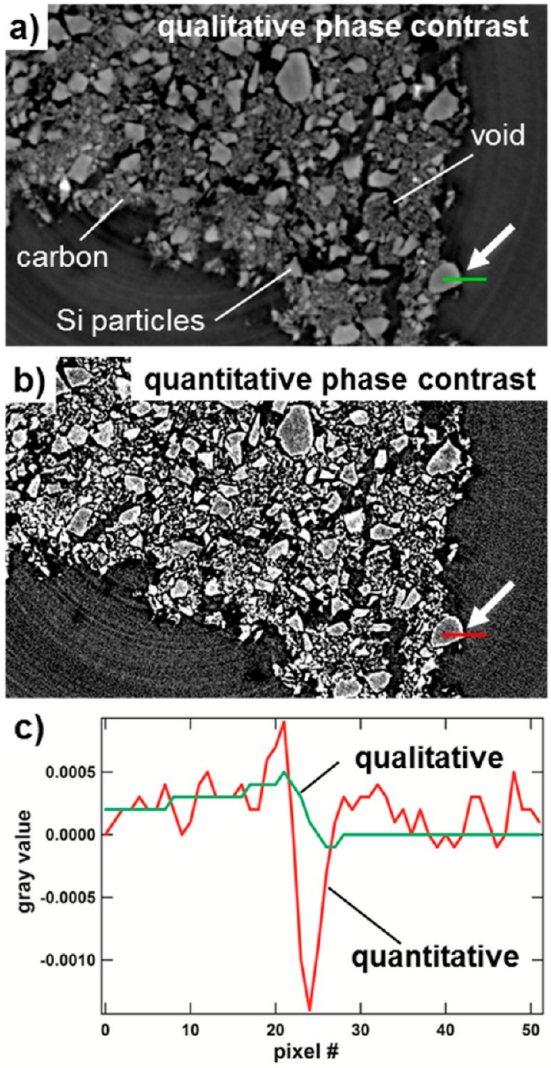

Figure 7. A comparison between (a) a qualitative phase-contrast tomography reconstructed slice and (b) a quantitative phase-contrast tomography reconstruction of that exact same slice. (c) The green and red line scans highlight the transition across the particle−void interface in (a) and (b), respectively.

also a 267% change in thickness (z-direction) from the pristine electrode (60 μm) to the post-mortem electrode (160 μm). Notice the large difference in the SEM/caliper estimated thickness (~80 μm) and the true value measured with tomography. The initial and post-mortem microtomographs can also be analyzed in terms of porosity, SA/V, and tortuosity albeit limited by the system resolution. Indeed, the importance of nanoscale features on electrode-level porosity, tortuosity, and surface area has been demonstrated by several authors.[46,58,59] Assuming that both the Si and carbonaceous material are nonporous, the pristine electrode porosity is 58% (void volume) and this value decreases after cycling with post-mortem electrode porosity estimated at 46% (N = 2). This decrease in porosity, despite the increase in electrode volume, is likely due to poor particle packing and SEI formation which swells the electrode and electrically isolates the smaller Si particles. This hypothesis is supported by the increase in carbonaceous material volume ratio within the electrode from 14% to 44% (N = 2) for the pristine and cycled electrodes, respectively. The SA/V ratio of the Si particles increases from

dx.doi.org/10.1021/am5003124 | ACS Appl. Mater. Interfaces 2014, 6, 4524−4534

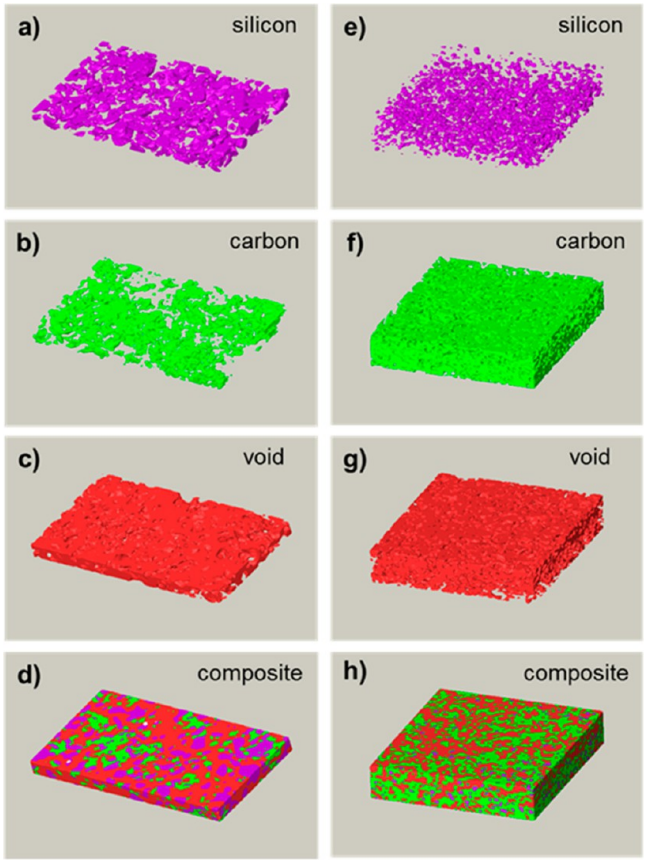

Figure 8. Segmented microtomographs of the pristine (a–d) and cycled (e–h) Si laminate electrodes. The left column shows the distribution of (a) the Si particles (purple), (b) carbonaceous materials (green), and (c) voids (red) within the pristine electrode as well as (d) all the components merged together. The right column shows the distribution of (e) the Si particles, (f) carbonaceous materials, and (g) voids within the cycled electrode as well as (h) all the components merged together.

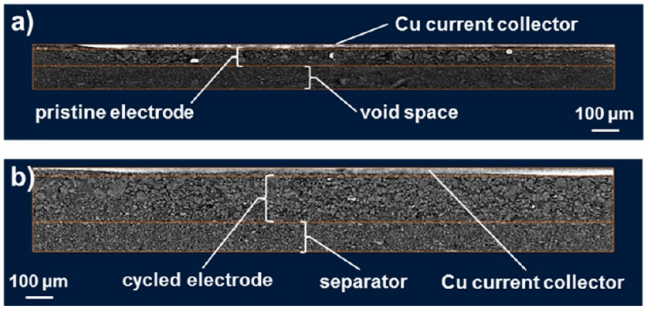

Figure 9. Orthoslices of (a) pristine and (b) cycled Si laminate electrodes generated from MicroCT imaging. A qualitative thickness comparison of the pristine and cycled Si laminate electrodes where the pristine electrode is ca. 60 μm, whereas the cycled electrode is ca. 160 μm.

0.42 to 0.71 which is in line with decreasing particle size. When the Si laminate data is compared to the Cu_6Sn_5 on Cu foam data, perhaps the most significant finding from this study is the difference in *z*-axis expansion. Whereas the laminate showed a 267% change in this direction, the foam, as expected, showed no change. This comparison signifies the importance of distributed current collection in thick electrode formats for high capacity anode materials.

4. CONCLUSION

Herein, we have shown the development of synchrotron microtomography at the 2-BM beamline of the Advanced Photon Source. *In situ* and *ex situ* investigations of the change in volume specific surface area for Cu_6Sn_5 on Cu foam electrodes and Si laminate electrodes were performed, respectively. At this time, this report represents the first *in situ* full field microtomography performed on a high capacity Li-ion battery anode. The normalized SA/V ratio of Cu_6Sn_5 active material on Cu foam increased with cycling by 10–15% with no changes in the thickness of the electrode. The Si laminate data shows a different result. The components of the Si laminate were qualitatively and quantitatively distinguished, and the changes in the volume fraction of different materials were calculated. An increase in carbonaceous material was discovered throughout the entire thickness of the electrode, along with a drastic increase in the overall laminate thickness. The determination of physical parameters afforded by this technique (SA/V, porosity) should prove useful to the modeling and simulations community. The differences in electrode architecture and their resulting expansion, or lack thereof, is notable for electrode design considerations. Future studies will focus on improving the beamline cell design (e.g., better regulated stack pressure) and enhancing the capabilities of the 2-BM setup (e.g., higher spatial resolution).

■ ASSOCIATED CONTENT

Supporting Information

Pristine and post-mortem SEM images of the Cu_6Sn_5 on Cu foam and the Si laminate electrodes, microtomographs of the foam electrode at different points in the cell cycle life, and additional electrochemical data from the beamline cells. This information is available free of charge via the Internet at http://pubs.acs.org/.

■ AUTHOR INFORMATION

Corresponding Authors

*E-mail: brushett@mit.edu.
*E-mail: trahey@anl.gov.

Notes

The authors declare no competing financial interest.

■ ACKNOWLEDGMENTS

Support from the Vehicle Technologies Program, Hybrid and Electric Systems, in particular David Howell and Tien Duong at the U.S. Department of Energy, Office of Energy Efficiency and Renewable Energy, is gratefully acknowledged. The submitted manuscript has been created by UChicago Argonne, LLC, Operator of Argonne National Laboratory ("Argonne"). Argonne, a U.S. Department of Energy Office of Science Laboratory, is operated under Contract No. DE-AC02-06CH11357. Use of the Advanced Photon Source, an Office of Science User Facility operated for the U.S. Department of Energy (DOE) Office of Science by Argonne National Laboratory, was supported by the U.S. DOE under Contract No. DE-AC02-06CH11357. F.R.B. was supported by a Director's Postdoctoral Fellowship. The authors thank Sharece Corner for assistance in manuscript preparation.

■ REFERENCES

(1) Armand, M.; Tarascon, J.-M. Building better batteries. *Nature* **2008**, *451*, 652–657.

(2) United States Advanced Battery Consortium, Electrochemical Energy Storage Technical Team Technology Development Roadmap, July 7th, 2006, http://www1.eere.energy.gov/vehiclesandfuels/pdfs/program/electrochemical_energy_storage_roadmap.pdf.
(3) Thackeray, M. M.; Wolverton, C.; Isaacs, E. D. Electrical energy storage for transportation—approaching the limits of, and going beyond, lithium-ion batteries. *Energy Environ. Sci.* **2012**, *5*, 7854−7863.
(4) Trahey, L.; Kung, H. H.; Thackeray, M. M.; Vaughey, J. T. Effect of electrode dimensionality and morphology on the performance of Cu2Sb thin film electrodes for lithium-ion batteries. *Eur. J. Inorg. Chem.* **2011**, *26*, 3984−3988.
(5) Liu, G.; Xun, S.; Vukmirovic, N.; Song, X.; Olalde-Velasco, P.; Zheng, H.; Battaglia, V. S.; Wang, L.; Yang, W. Polymers with tailored electronic structure for high capacity lithium battery electrodes. *Adv. Mater.* **2011**, *23*, 4679−4683.
(6) Qiao, H.-B.; Tian, X.-M.; Yi, T.-F. Electrochemical properties of Si negative electrodes bonded with partially hydrolyzed polyacrylamide for Li-ion batteries. *Int. J. Electrochem. Sci.* **2013**, *8*, 9414−9420.
(7) Li, J.; Le, D.-B.; Ferguson, P. P.; Dahn, J. R. Lithium polyacrylate as a binder for tin-cobalt-carbon negative electrodes for lithium-ion batteries. *Electrochim. Acta* **2010**, *55*, 2991−2995.
(8) Gao, Y. F.; Zhou, M. Strong stress-enhanced diffusion in amorphous lithium alloy nanowire electrodes. *J. Appl. Phys.* **2011**, *109*, 014310.
(9) Zhou, Y.-N.; Xue, M.-Z.; Fu, Z.-W. Nanostructured thin film electrodes for lithium storage and all-solid-state thin-film lithium batteries. *J. Power Sources* **2013**, *234*, 310−332.
(10) Liu, B.; Soares, P.; Checkles, C.; Zhao, Y.; Yu, G. Three-dimensional hierarchal ternary nanostructures for high-performance Li-ion battery anodes. *Nano Lett.* **2013**, *13*, 3414−3419.
(11) Ke, F.-S.; Huang, L.; Solomon, B. C.; Wei, G.-Z.; Xue, L.-J.; Zhang, B.; Li, J.-T.; Zhou, X.-D.; Sun, S.-G. Three-dimensional nanoarchitecture of Sn-Sb-Co alloy as an anode of lithium-ion batteries with excellent lithium storage performance. *J. Mater. Chem.* **2012**, *22*, 17511−17517.
(12) Trahey, L.; Vaughey, J. T.; Kung, H. H.; Thackeray, M. M. High-capacity, microporous Cu_6Sn_5-Sn anodes for Li-ion batteries. *J. Electrochem. Soc.* **2009**, *156*, A385−A389.
(13) Jiang, T.; Zhang, S.; Lin, R.; Liu, G.; Liu, W. Electrochemical characterization of cellular Si and Si/C anodes for lithium-ion battery. *Int. J. Electrochem. Sci.* **2013**, *8*, 9644−9651.
(14) Shin, H.-C.; Liu, M. Three-dimensional porous copper-tin alloy electrodes for rechargeable lithium batteries. *Adv. Funct. Mater.* **2005**, *15*, 582−586.
(15) Goldman, J. L.; Long, B. R.; Gewirth, A. A.; Nuzzo, R. G. Strain anistropies and self-limiting capacities in single-crystalline 3D silicon microstructures: Models for high energy density lithium-ion battery anodes. *Adv. Funct. Mater.* **2011**, *21*, 2412−2422.
(16) Chakrapani, V.; Rusli, F.; Filler, M. A.; Kohl, P. A. Silicon nanowire anode: Improved battery life with capacity-limited cycling. *J. Power Sources* **2012**, *205*, 433−438.
(17) Ebner, M.; Geldmacher, F.; Marone, F.; Stampanoni, M.; Wood, V. X-ray tomography of porous, transition metal oxide based lithium ion battery electrodes. *Adv. Energy Mater.* **2013**, *3*, 845−850.
(18) Wilson, J. R.; Cronin, J. S.; Barnett, S. A.; Harris, S. J. Measurement of three-dimensional microstructure in a $LiCoO_2$ positive electrode. *J. Power Sources* **2011**, *196*, 3443−3447.
(19) Ender, M.; Joos, J.; Carraro, T.; Ivers-Tiffée, E. Three-dimensional reconstruction of a composite cathode for lithium-ion cells. *Electrochem. Commun.* **2011**, *13*, 166−168.
(20) Wilson, J. R.; Kobsiriphat, W.; Mendoza, R.; Chen, H.-Y.; Hiller, J.-M.; Miller, D.-J.; Thornton, K.; Voorhees, P. W.; Alder, S. B.; Barnett, S. A. Three-dimensional reconstruction of a solid-oxide fuel-cell anode. *Nat. Mater.* **2006**, *5*, 541−544.
(21) Su, Q.; Xie, D.; Zhang, J.; Du, G.; Xu, B. In situ transmission electron microscopy observation of the conversion mechanism of Fe_2O_3/graphene anode during lithiation-delithiation processes. *ACS Nano* **2013**, *7*, 9115−9121.
(22) Huang, B.; Tai, K. P.; Dillon, S. J. Structural evolution of α-Fe_2O_3 nanowires during lithiation and delithiation. *J. Power Sources* **2014**, *245*, 308−314.
(23) Ati, M.; Sathiya, M.; Boulineau, S.; Reynaud, M.; Abakumov, A.; Rousse, G.; Melot, B.; Van Tendeloo, G.; Tarascon, J.-M. Understanding and promoting the rapid preparation of the triplite-phase of $LiFeSO_4F$ for use as a large-potential Fe cathode. *J. Am. Chem. Soc.* **2012**, *134*, 18380−18387.
(24) Chen-Wiegart, Y.-C. K.; Cronin, J. S.; Yuan, Q.; Yakal-Kremski, K.-J.; Barnett, S. A.; Wang, J. 3D Non-destructive morphological analysis of a solid oxide fuel cell anode using full-field X-ray nano-tomography. *J. Power Sources* **2012**, *218*, 348−351.
(25) Ostadi, H.; Rama, P.; Liu, Y.; Chen, R.; Zhang, X.; Jiang, K. Nanotomography based study of gas diffusion layers. *Microelectron. Eng.* **2010**, *87*, 1640−1642.
(26) Epting, W. K.; Gelb, J.; Litster, S. Resolving the three-dimensional microstructure of polymer electrolyte fuel cell electrodes using nanometer-scale X-ray computed tomography. *Adv. Funct. Mater.* **2012**, *22*, 555−560.
(27) Gu, M.; Parent, L. R.; Mehdi, B. L.; Unocic, R. R.; McDowell, M. T.; Sacci, R. L.; Xu, W.; Connell, J. G.; Xu, P.; Abellan, P.; Chen, X.; Zhang, Y.; Perea, D. E.; Evans, J. E.; Lauhon, L. J.; Zhang, J. G.; Liu, J.; Browning, N. D.; Cui, Y.; Arslan, I.; Wang, C. M. Demonstration of an electrochemical liquid cell for operando transmission electron microscopy observation of the lithiation/delithiation behavior of Si nanowire battery anodes. *Nano Lett.* **2013**, *13*, 6106−6112.
(28) Schneider, A.; Wiser, C.; Roth, J.; Helfen, L. Impact of synchrotron radiation on fuel cell operation in imaging experiments. *J. Power Sources* **2010**, *195*, 6349−6355.
(29) Roth, J.; Eller, J.; Büchi, F. N. Effects of synchrotron radiation on fuel cell materials. *J. Electrochem. Soc.* **2012**, *159*, F449−F455.
(30) Sinha, P. K.; Halleck, P.; Wang, C.-Y. Quantification of liquid water saturation in a PEM fuel cell diffusion medium using X-ray microtomography. *Electrochem. Solid-State Lett.* **2006**, *9*, A344−A348.
(31) Eller, J.; Rosén, T.; Marone, F.; Stampanoni, M.; Wokaun, A.; Büchi, F. N. Progress in in situ X-ray tomographic microscopy of liquid water in gas diffusion layers of PEFC. *J. Electrochem. Soc.* **2011**, *158*, B963−B970.
(32) Becker, J.; Flückiger, R.; Reum, M.; Büchi, F. N.; Marone, F.; Stampanoni, M. Determination of materials properties of gas diffusion layers: Experiments and simulations using phase contrast tomographic microscopy. *J. Electrochem. Soc.* **2009**, *156*, B1175−B1181.
(33) Flückiger, R.; Marone, F.; Stampanoni, M.; Wokaun, A.; Büchi, F. N. Investigation of liquid water in gas diffusion layers of polymer electrolyte fuel cells using X-ray tomographic microscopy. *Electrochim. Acta* **2011**, *56*, 2254−2262.
(34) Kim, S.-G.; Lee, S.-J. Tomographic analysis of porosity variation in gas diffusion layer under freeze-thaw cycles. *Int. J. Hydrogen Energy* **2012**, *37*, 566−574.
(35) Krüger, P.; Markotter, H.; Haubmann, J.; Klages, M.; Arlt, T.; Banhart, J.; Hartnig, C.; Manke, I.; Scholta, J. Synchrotron X-ray tomography for investigations of water distribution in polymer electrolyte membrane fuel cells. *J. Power Sources* **2011**, *196*, 5250−5255.
(36) Fishman, Z.; Hinebaugh, J.; Bazylak, A. Microscale tomography investigations of heterogeneous porosity distributions of PEMFC GDLs. *J. Electrochem. Soc.* **2010**, *157*, B1643−B1650.
(37) Hinebaugh, J.; Fishman, Z.; Bazylak, A. Unstructured pore network modeling with heterogeneous PEMFC GDL porosity distributions. *J. Electrochem. Soc.* **2010**, *157*, B1651−B1657.
(38) Pfrang, A.; Veyret, D.; Janssen, G. J. M.; Tsotridis, G. Imaging of membrane electrode assemblies of proton exchange membrane fuel cells by X-ray computed tomography. *J. Power Sources* **2011**, *196*, 5272−5276.
(39) Jhong, H. R. M.; Brushett, F. R.; Yin, L. L.; Stevenson, D. M.; Kenis, P. J. A. Combining structural and electrochemical analysis of electrodes using micro-computed tomography and a microfluidic fuel cell. *J. Electrochem. Soc.* **2012**, *159*, B292−B298.

(40) Jhong, H. R. M.; Brushett, F. R.; Kenis, P. J. A. The effects of catalyst layer deposition methodology on electrode performance. *Adv. Energy Mater.* **2013**, *3*, 589−599.
(41) Fukunaga, H.; Kishimi, M.; Ozaki, T.; Sakai, T. Non-foam nickel electrode with quasi-three-dimensional substrate for Ni-MH battery. *J. Electrochem. Soc.* **2005**, *152*, A126−A131.
(42) Manke, I.; Banhart, J.; Haibel, A.; Rack, A.; Zabler, S.; Kardjilov, N.; Hilger, A.; Melzer, A.; Riesemeier, H. In situ investigation of the discharge of alkaline Zn-MnO_2 batteries with synchrotron X-ray and neutron tomographies. *Appl. Phys. Lett.* **2007**, *90*, 214102.
(43) Haibel, A.; Manke, I.; Melzer, A.; Banhart, J. In situ microtomographic monitoring of discharging processes in alkaline cells. *J. Electrochem. Soc.* **2010**, *157*, A387−A391.
(44) Shearing, P. R.; Howard, L. E.; Jørgensen, P. S.; Brandon, N. P.; Harris, S. J. Characterization of the 3-dimensional microstructure of a graphite negative electrode from a Li-ion battery. *Electrochem. Commun.* **2010**, *12*, 374−377.
(45) Yufit, V.; Shearing, P.; Hamilton, R. W.; Lee, P. D.; Wu, M.; Brandon, N. P. Investigation of lithium-ion polymer battery cell failure using X-ray computed tomography. *Electrochem. Commun.* **2011**, *13*, 608−610.
(46) Shearing, P. R.; Brandon, N. P.; Gelb, J.; Bradley, R.; Withers, P. J.; Marquis, A. J.; Cooper, S.; Harris, S. J. Multi length scale microstructural investigations of a commercially available Li-ion battery electrode. *J. Electrochem. Soc.* **2012**, *159*, A1023−A1027.
(47) Shearing, P.; Wu, Y.; Harris, S. J.; Brandon, N. In situ X-ray spectroscopy and imaging of battery materials. *ECS Interface* **2011**, *20*, 43−47.
(48) Bentzen, S. M. Evaluation of the spatial resolution of a CT scanner by direct analysis of the edge response function. *Med. Phys.* **1983**, *10*, 579−581.
(49) Smith, S. W. *Digital signal processing: A practical guide for engineers and scientists*. Elsevier Science Newnes: London, 2003.
(50) Hussein, E. M. A. *Computed Radiation Imaging: Physics and Mathematics of Forward and Inverse Problems*; Elsevier: London, 2011.
(51) Dowd, B. A.; Campbell, G. H.; Marr, R. B.; Nagarkar, V.; Tipnis, S.; Axe, L.; Siddons, D. P. Developments in synchrotron X-ray computed microtomography at the National Synchrotron Light Source. *Proc. SPIE* **1999**, *3772*, 224−236.
(52) Marone, F.; Stampanoni, M. Regridding reconstruction algorithm for real-time tomographic imaging. *J. Synchrotron Radiat.* **2012**, *19*, 1029−1037.
(53) Paganin, D.; Mayo, S. C.; Gureyev, T. E.; Miller, P. R.; Wilkins, S. W. Simultaneous phase and amplitude extraction from a single defocused images of a homogeneous object. *J. Microsc.* **2002**, *206*, 33−40.
(54) Sharma, S.; Fransson, L.; Sjöstedt, E.; Nordström, L.; Johansson, B.; Edström, K. A theoretical and experimental study of the lithiation of η' Cu_6Sn_5 in a lithium-ion battery. *J. Electrochem. Soc.* **2003**, *150*, A330−A334.
(55) Kepler, K. D.; Vaughey, J. T.; Thackeray, M. M. $Li_xCu_6Sn_5$ ($0 < x < 13$): An intermetallic insertion electrode for rechargeable lithium batteries. *Electrochem. Solid-State Lett.* **1999**, *2*, 307−309.
(56) Shkrob, I. A.; Zhu, Y.; Marin, T. W.; Abraham, D. Reduction of carbonate electrolytes and the formation of solid-electrolyte interface (SEI) in lithium-ion batteries. 2. Radiolytically induced polymerization of ethylene carbonate. *J. Phys. Chem. C.* **2013**, *117*, 19270−19279.
(57) Ryu, J. H.; Kim, J. W.; Sung, Y.-E.; Oh, S. M. Failure modes of silicon powder negative electrode in lithium secondary batteries. *Electrochem. Solid-State Lett.* **2004**, *7*, A306−A309.
(58) Vijayaraghavan, B.; Ely, D. R.; Chiang, Y.-M.; García-García, R.; García, R. E. An analytical method to determine tortuosity in rechargeable battery electrodes. *J. Electrochem. Soc.* **2012**, *159*, A548−A552.
(59) Thorat, I. V.; Stephenson, D. E.; Zacharias, N. A.; Zaghib, K.; Harb, J. N.; Wheeler, D. R. Quantifying tortuosity in porous Li-ion battery materials. *J. Power Sources* **2009**, *188*, 592−600.